communications earth & environment

Article

https://doi.org/10.1038/s43247-024-01710-2

Moisture variability in northeast Tibet following the middle Miocene Climate transition

Zhixiang Wang[1] ✉, Catherine D. Bradshaw[2,3], Haicheng Wei[1], Mengmeng Cao[4], Chunju Huang[4] ✉, Wenxia Han[1] ✉ & Jordan T. Abell[5,6]

After the middle Miocene Climate transition, global cooling caused substantial hydrological changes in East Asia. Today, many lines of evidence indicate that inland East Asia experienced persistent aridification after the middle Miocene Climate transition. However, chemical weathering records from the South China Sea as well as late-Miocene paleolake expansions in northeastern Tibet contrast with the idea of long-term aridification after the middle Miocene Climate transition. Here, we present manganese-to-iron ratios and clay mineral contents of sediments formed approximately 14 to 10 million years ago from the Guide Basin, northeastern Tibetan Plateau, combined with previously published records (lithology, magnetic susceptibility, redness, and strontium content). Our results show that a paleolake in the Guide Basin expanded between approximately 11.4 and 10.5 million years ago, opposite to the long-term drying trend after the middle Miocene Climate transition. On the 100-kilo-year eccentricity scale, our results demonstrate alternating moisture source variability in northeast Tibet, with precipitation predominantly delivered via the westerlies and the East Asian summer monsoon. This variability could potentially be related to the movement of the westerly jet over the Tibetan Plateau. After comparison to climate model simulations, we attribute this movement to astronomical forcing and the waxing and waning of the Antarctic ice sheet.

The Middle Miocene Climatic Optimum (~17–14 million years ago) encompasses an interval of relatively warmer temperatures and enhanced precipitation during the mid-Miocene[1–4]. This period was immediately followed by the Middle Miocene Climate Transition, which was characterized by a global sea level drop of ~40–90 m[5–7], a cooling of ~6–7 °C and ~2 °C for sea surface temperatures near Antarctica and in the Equatorial Pacific, respectively[8–10], and a pCO_2 decrease of ~100 ppm[11,12]. This substantial global cooling and the permanent establishment of the East Antarctic ice sheet likely had an influence on global precipitation, sea and land surface temperatures, oceanic circulation, and the biosphere[13–16]. Despite this cooling and its potential ramifications, the mechanisms behind it are still debated, with orbital forcing, reorganization of past ocean circulation, and/or atmospheric CO_2 drawdown all having been proposed to trigger the middle Miocene Climate transition[8,9,11,17,18].

The hydrological cycle of East Asia was altered across the middle Miocene Climate transition via impacts from shifts in the location of the tropical rain belt[13], intensification of Atlantic and/or global Meridional Overturning Circulation[14,19,20], varied meridional heat/water vapor transport[21,22] and decreased global sea-level[23]. Specifically, pollen records[24,25], magnetic proxies[26,27], geochemical element concentrations[28], and carbonate oxygen isotopes[29] all suggest that the relatively humid environment of inland Asia around 17–15 million years ago became arid after the middle Miocene Climate transition. However, these results contrast with proxy records from South China Sea sediments[30] and expansion of paleolakes in the Guide, Xunhua and Linxia basins[31,32], which imply increased summer monsoonal precipitation in East Asia around 11–10 million years ago. Modeling results may support this notion, as simulations with an expanded Antarctic ice sheet but no Greenland ice sheet show enhanced summer monsoon precipitation in East Asia[33]. Considering the discrepancies between prior studies, the long-term evolution of East Asian hydroclimate variability is still uncertain.

Sediments from Northeast (NE) Tibet can provide sensitive archives of past changes in the regional hydroclimate of East Asia related to the middle

[1]Qinghai Provincial Key Laboratory of Geology and Environment of Salt Lakes, Qinghai Institute of Salt Lakes, Chinese Academy of Sciences, Xining, 810008, China. [2]The Global Systems Institute, University of Exeter, Exeter, UK. [3]Met Office Hadley Centre, Exeter, UK. [4]School of Earth Sciences, China University of Geosciences, Wuhan, China. [5]Department of Earth and Environmental Sciences, Lehigh University, Bethlehem, PA, 18015, USA. [6]Department of Geosciences, University of Arizona, Tucson, AZ, 85721, USA. ✉e-mail: wangzhi8905@126.com; huangcj@cug.edu.cn; wenxia_han@163.com

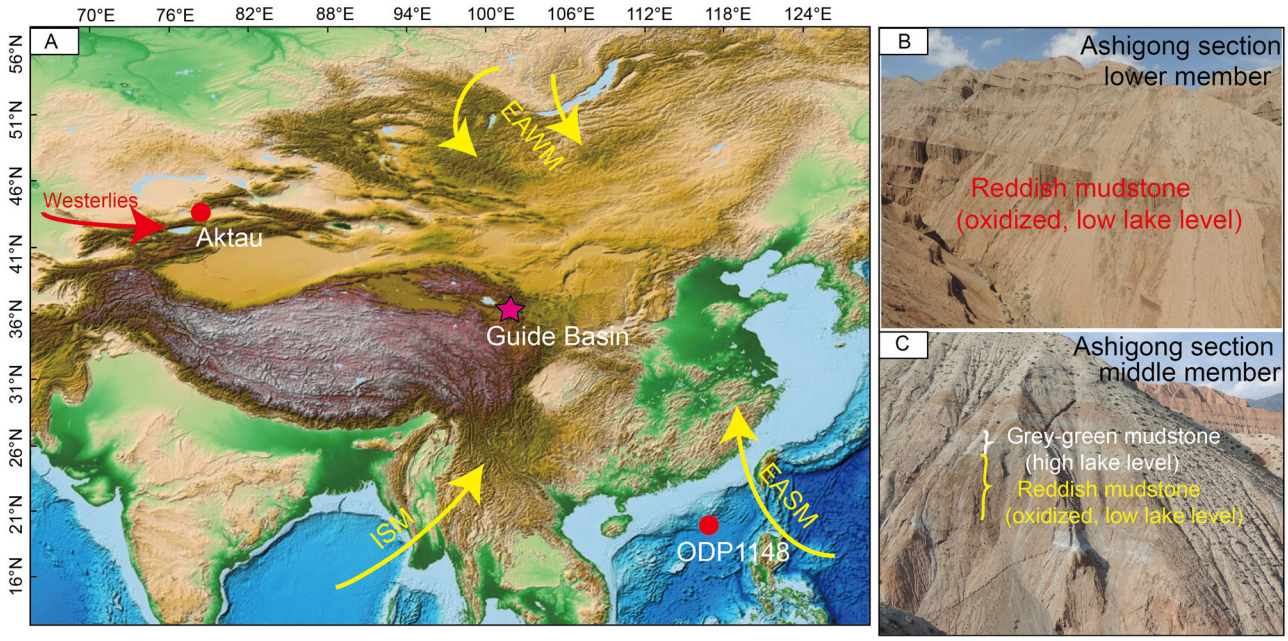

Fig. 1 | Map showing the locations of the Guide Basin (this study), Aktau Section[55] and marine sediment core ODP 1148[30]. **A** The Aktau Section is in the arid zone predominantly influenced by moisture derived from the westerlies. The Ashigong Section in the Guide Basin receives precipitation from both the westerlies and the East Asian summer monsoon. Finally, ODP 1148 is proximal to East Asian summer monsoon moisture sources. The base map was taken from https://www.ngdc.noaa.gov/mgg/global/ that is a globally shareable website. **B**, **C** are field photographs from the Guide Section. EAWM-East Asian winter monsoon; EASM-East Asian summer monsoon; ISM-Indian summer monsoon.

Miocene Climate transition[34,35]. Specifically, they potentially allow for the discernment of orbital-scale shifts in the contribution of precipitation between moisture delivered via the westerlies from Central Asia and East Asian summer monsoon-related moisture coming from the Pacific Ocean and the South China Sea during and after this important interval of the geologic past[32,36]. However, previous studies in NE Tibet have primarily focused on the long-term, million-year climate evolution of this region, and lack sufficiently high-resolution paleohydrological records spanning the middle-to-late Miocene. Here we present orbital-scale geochemical records of element concentrations and clay mineral ratios for the interval of ~13.7–10 million years ago from the Guide Basin, located on the NE Tibetan margin, and interpret our data with the aid of recent climate model simulations for the Middle Miocene[37]. Our results reveal an antiphase relationship between westerly moisture contribution and East Asian summer monsoon-derived moisture on 100-kyr timescales.

Results and discussion

Orbital cycles in Middle Miocene hydroclimate records on the NE Tibet

The Guide Basin is surrounded by the Waligong Shan to the west, the Zamazari Shan to the east, the Laji Shan to the north, and the West Qinling Mountains to the south (Fig. 1). The Neogene deposits of the Guide Basin have been divided into the Guidemen (~20.8–19 million years ago), Garang (~19– < 16 million years ago), Ashigong (~> 11.5–7.8 million years ago), Heerjia (~7.8–3.6 million years ago), and Ganjia (~3.6–2.6 million years ago) formations based on a combination of magneto- and mammalian stratigraphy[32,38]. The middle Miocene Ashigong Formation is composed of massive red-brown, blocky mudstones interbedded with grayish-green, finely-laminated mudstones, sandstones, and siltstones in the lower member, changing to deposits dominated by marls and gypsum-rich grayish-green mudstones in the middle member, and finally prominent, dense red-brown and grayish-green mudstones in the upper member[32]. The lower and upper members indicate a marginal lake depositional environmental, while the middle member reflects a more permanent lake setting[32]. A recent age model constructed for the Ashigong Section in the Guide Basin spanning ~13.7–10 million years ago suggests a dominant ~100 kyr cyclicity in the Guide paleolake evolution[32]. The age uncertainties of the Ashigong Section are based on the paleomagnetic boundary uncertainties, with about ± 40 kyr error in pairs of normal+reversed polarity[32]. Recently, Yao et al.[39] used the lightness (L*) of the Ashigong Formation sediments for astronomical tuning using the magnetostratigraphy as initial constraints. Specifically, these authors correlated the ~50 m wavelengths in the L* series to the orbital eccentricity metronome. Their tuning results indicate the presence of 405 kyr spectral peaks with high significance as well as ~100 kyr, 40 kyr and 20 kyr spectral peaks in the L* series. In particular, the ~100-kyr cycles in the L* are antiphase with the La2004 short orbital eccentricity model[39]. These findings suggest that our interpretations regarding moisture-derived variability, at least on the 100-kyr orbital scale, are robust.

We measured several proxies to reconstruct hydroclimate variability in the Ashigong Formation in the Guide Basin, including manganese-to-iron ratios (Mn/Fe, ~10 cm sampling resolution) and clay mineral content (~1 m sampling resolution) (Figs. 2 and 3). In sediment porewaters, Mn reduction occurs prior to Fe reduction as oxygen is depleted, and as such lower Mn/Fe rations typically indicate reducing conditions while elevated Mn/Fe ratios point to more oxygenated porewaters[40–42]. In the Ashigong Section, periods of low magnetic susceptibility (MS) and redness and high Mn/Fe correspond to intervals of gray-green mudstone. Individually, Fe content is generally low and Mn is relatively high (Fig. 2 and Supplementary Fig. S1) within these gray-green mudstone layers. Broadly, the trends in Mn/Fe ratios, redness, and MS are consistent. Therefore, we suggest that the Mn/Fe ratios can reflect the sedimentary environment during the mid-to-late Miocene, and specifically indicate regional lake level fluctuations (Fig. 2 and Supplementary Fig. S1). While the correspondence between Mn/Fe ratios and lake level may seem counterintuitive, we suggest that increased regional precipitation, and in turn elevated lake levels, resulted in *i*) enhanced post-depositional dissolution of Fe-bearing magnetic minerals, *ii*) precipitation of Mn carbonates, or *iii*) a combination of these two processes, ultimately increasing Mn/Fe ratios on these layers. Post-depositional dissolution of Fe-bearing magnetic minerals is common in lacustrine deposits of northern Chinese basins[22,43] (Supplementary text 1). In summary, based on other data from the section and

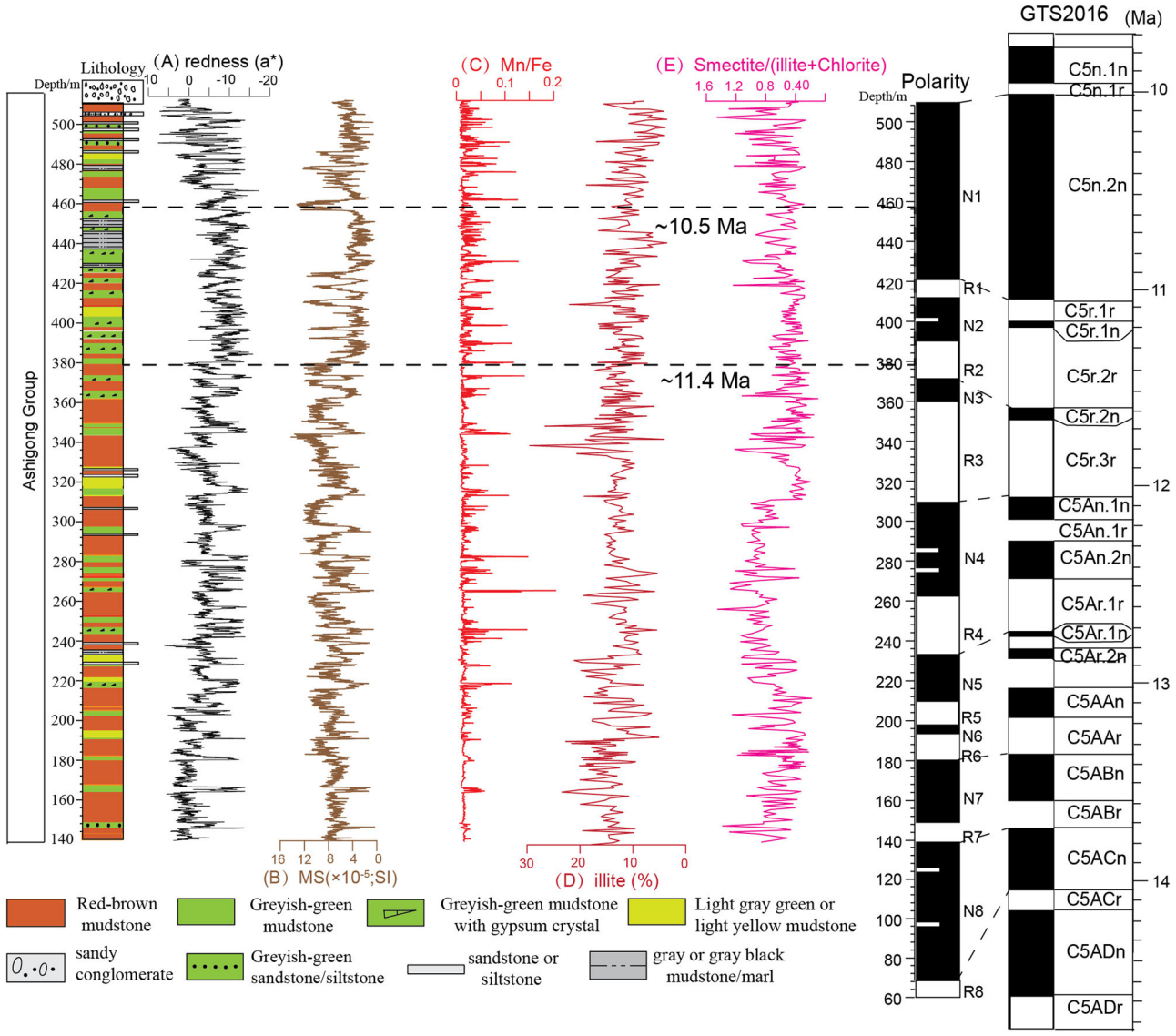

Fig. 2 | Lithology, magnetic stratigraphy and paleoclimate proxies of the Ashigong Formation in the Guide Basin, NE Tibet. (**A**) redness (a*). (**B**) magnetic susceptibility (MS). (**C**) Mn/Fe ratios. (**D**) illite content, and (**E**) smectite/(illite+chlorite) ratios. Magnetic stratigraphy, redness and MS data are from Wang et al.[32].

our posited diagenetic impacts, we assume that higher Mn/Fe ratios in our record generally correlate to higher lake levels and are linked to periods with higher regional precipitation.

In certain environments (i.e., regions and time periods where provenance changes are minimized), clay mineralogy can be used to reconstruct the silicate weathering intensity of the larger catchment[44,45]. Chlorite and illite primarily reflect cold and/or arid environments, whereas smectite indicates temperate-humid climates[45]. Thus, higher smectite/(illite+chlorite) ratios generally represent periods with stronger chemical weathering resulting from either higher temperature, precipitation, or a combination thereof. According to the classical diagenesis model by Weaver[46], when digenesis plays a major role in regulating illite and smectite contents, the illite content is expected to exhibit gradual increases with the rise of the burial depth. Our results show that illite is relatively stable and does not show an obvious change with depth (Fig. 2 and Supplementary Fig. S1), suggesting minimal diagenetic impacts during and after deposition of the studied Ashigong Section.

Evolutive spectral analysis of our Mn/Fe proxy displays dominant ~100-kyr cycles between ~13.7 and 10 million years ago (Fig. 3). We interpret these ~100-kyr cycles to represent eccentricity-forced paleolake level/precipitation variability in the Guide Basin during the period of ~13.7-10 million years ago[32]. Additionally, our smectite/(illite+chlorite) record contains prominent ~405-kyr and ~100-kyr cycles throughout the period of ~13.7–10 million years ago (Supplementary Fig. S2). Both the Mn/Fe and smectite/(illite+chlorite) records display weak obliquity (41-kyr) and precession (23- and 19-kyr) signals (Fig. 3 and Supplementary Fig. S2). It could be argued that the lack of 41-kyr, 23-kyr, and/or 19-kyr cycles in the two records, particularly the lower resolution clay mineral ratios, may be an artifact of sampling resolution. Sedimentation rates based on magnetic reversal stratigraphy are approximately 6.5–14.4 cm/kyr[32]. This leads to sampling intervals spanning ~0.7–1.5 kyr for Mn/Fe and ~7–15.4 kyr for the clay mineral ratios. However, even in the interval containing the highest sedimentary rates (~14.4 cm/kyr; ~11.6–12.1 million years ago), the 100-kyr cycles are still dominant compared to either obliquity or precession signals (Fig. 3 and Supplementary Fig. S2). As such, we suggest that the findings of our spectral analysis for both proxy records are robust. Finally, we note that the Mn/Fe ratio shows a stronger obliquity signal between 12.4 and 13 million years ago compared to the clay mineral ratios (Fig. 3). This difference in orbital expression between the Mn/Fe and smectite/(illite+chlorite) data may be attributed to the fact that variability in the smectite/(illite+chlorite) ratio is not only affected by precipitation, but can also be linked to changes in temperature as well as biological activity[44,45].

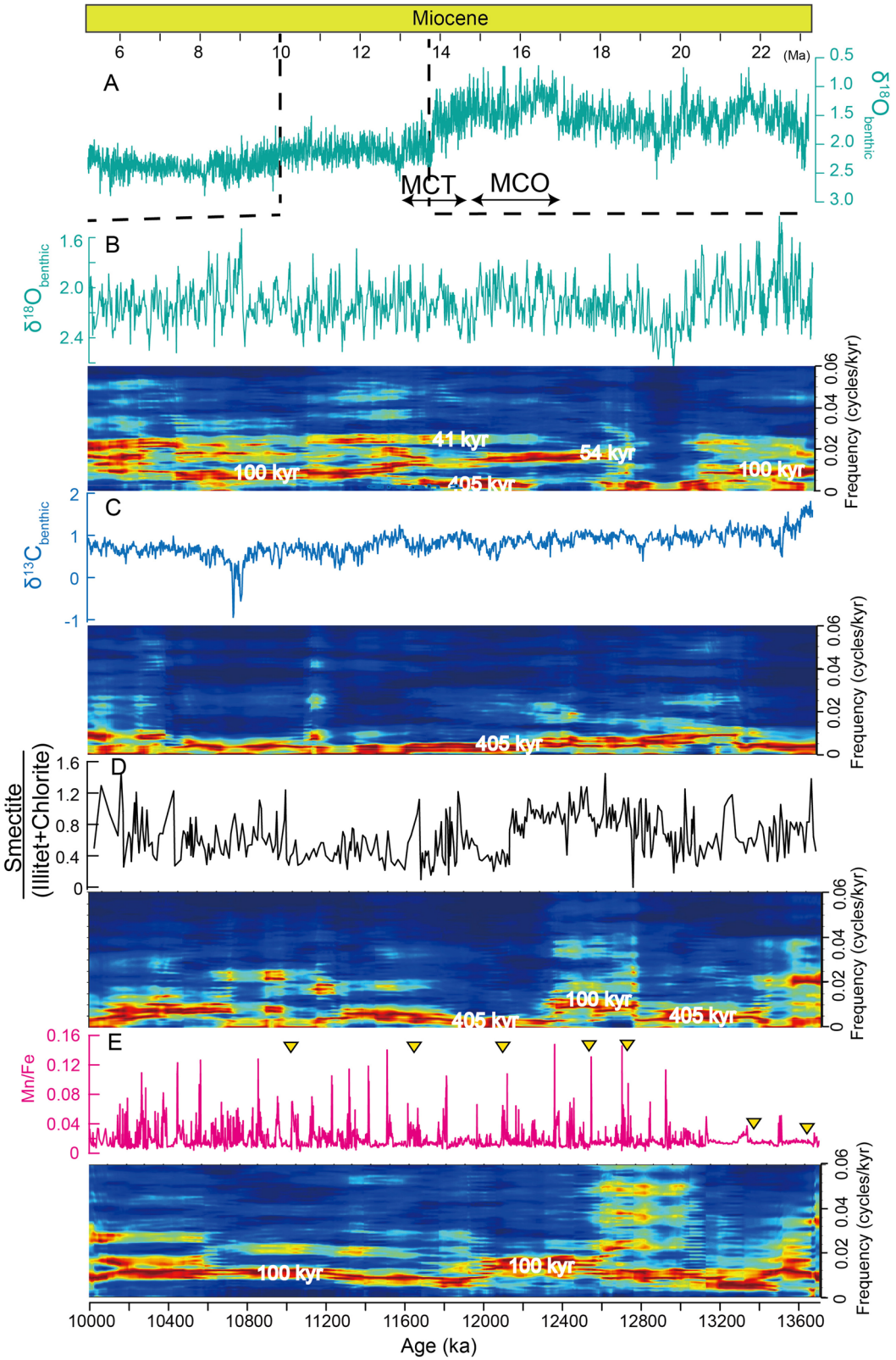

Fig. 3 | Evolutionary spectra of global $\delta^{18}O_{benthic}$, $\delta^{13}C_{benthic}$, smectite/(illite+chlorite) and Mn/Fe ratios over the period of ~13.7–10 Ma. A Global $\delta^{18}O_{benthic}$ timeseries across the Miocene[64]. **B** Global $\delta^{18}O_{benthic}$ timeseries for the interval of ~13.7–10 Ma[64]. **C** Global $\delta^{13}C_{benthic}$ time series for the interval of ~13.7–10 Ma[72]. **D** Smectite/(illite+chlorite) ratio from the Guide Section spanning ~13.7–10 Ma (this study). **E** Mn/Fe ratios from the Guide Section spanning ~13.7–10 Ma (this study). The yellow inverted triangles are the paleomagnetic age tie-points. MCT Miocene Climate transition, MCO Miocene Climatic Optimum.

Sources of water vapor for NE Tibet across ~ 14–10 million years ago

A comprehensive review of pedogenic and lacustrine carbonate stable oxygen isotope data in Asia shows that south Asian monsoonal-derived moisture has not been transported toward the Central Tibetan Plateau since the Cenozoic[47,48]. Thus, the hydrological budget of the NE Tibet is a balance of East Asian summer monsoonal moisture originating from the Pacific Ocean and the South China Sea, and winter, westerly-derived moisture from the North Atlantic and the Mediterranean[48,49]. Analyses of pollen records from the late-Oligocene Lanzhou Basin[50], temporal-spatial distributions of carbonate $\delta^{18}O$ and $\delta^{13}C$ across Asia[47], and late Oligocene-early Miocene eolian deposits in the Tianshui Basin[51] suggest that NE Tibet predominantly experienced a monsoonal climate like that of the present day since the late Oligocene, with a smaller contribution of moisture delivered via the westerlies. Although some thermochronological data and sedimentary records reveal that the Pamir Mountains experienced substantial uplift prior to the early Miocene and thus acted as an important barrier to precipitation in inland Asia[36,52], an open channel between the Pamir Mountains and the Tianshan Mountains may have existed during the middle Miocene[53]. As such, moisture brought from the westerlies could have penetrated the Tarim Basin and/or the Qaidam Basin at this time[53,54], indicating that previous studies may have underestimated the contribution of westerlies-derived moisture to NE Tibet.

To explore moisture sources and orbital-scale moisture variability of the NE Tibet during the interval of ~14–10 million years ago, we utilize hematite/goethite records from Ocean Drilling Program (ODP) 1148 in the South China[30] (Fig. 1), which lies near East Asian summer monsoon moisture sources, and $CaSO_4$ contents from the Aktau Section in the Ili Basin, which receives moisture predominantly via the westerlies[55] (Fig. 1). In a lake system, a low $CaSO_4$ content reflects enhanced aquifer recharge and is associated with lake freshening accompanied by rising lake levels, whereas a high $CaSO_4$ content is related to a negative water budget and higher solute concentration[55]. Hematite/goethite records from marine sediments may reflect continental chemical weathering processes because during soil formation, humid conditions are favorable for goethite formation while drier conditions are favorable for hematite formation[30]. For ODP 1148 in the South China Sea specifically, the hematite/goethite ratio is proposed to be a proxy for East Asian monsoonal precipitation variability based on two lines of evidence: 1) iron oxide formation and mineralogy in the source region are sensitive to East Asian summer monsoon precipitation[56,57], and 2) the influences of post-depositional redox changes on hematite/goethite ratios are limited as high-coercivity hematite and goethite are rather resistant to porewater reduction processes[56,57]. In addition, the hematite/goethite ratios from the ODP 1143 core correspond well with magnetic susceptibility of the Chinese Loess Plateau[58] (suggested to be a proxy of East Asian summer monsoon variability) during the late Pliocene[57]. Overall, more goethite deposition in the South China Sea corresponds to a stronger summer monsoon, whereas weaker summer monsoon periods would result in more hematite deposition[30,56,57]. Broadly, the hematite/goethite ratios from the South China Sea could reflect East Asian summer monsoon variability.

Hematite/goethite ratios in ODP 1148, $CaSO_4$ content of sediment from the Ili Basin (except for near zero values encountered in the interval of ~11.5–12.5 million years ago) and our Mn/Fe records reveal distinct ~100-kyr cycles, and imply a short eccentricity control of regional hydroclimate in the Middle Miocene (Fig. 4). This prominent ~100-kyr eccentricity signal is also recognized in hydrological records from the fluviolacustrine deposits in the Qaidam Basin, NE Tibet[21] (~8.5–7 million years ago), lake sediments from the Tianshui Basin, NE Tibet[22] (~10.25–8 million years ago), and fluviolacustrine sequences from the Weihe Basin, North China[59,60] (~ 5.2–2.6 million years ago). These suggest that the hydrological records across Asia are particularly sensitive to ~100-kyr eccentricity forcing under unipolar icehouse states.

The origin of an eccentricity control on Asian hydrological cycles prior to ~2.6 million years ago is suggested to be related to a non-linear amplification mechanism associated with Antarctic ice-sheet dynamics and/or eccentricity modulation of low-latitude summer insolation through a non-linear interaction with the global carbon cycle[21,22,60–62]. Inferred Middle Miocene high-water levels in the Guide and Ili basins correspond to low 405-kyr eccentricity intervals, which leads to decreased net incoming solar radiation to Earth's surface through its effect on precession amplitude (Fig. 4). At present, it is generally considered that the eccentricity maximum causes high-amplitude variability of precession cycle through amplitude modulation, enhancing the amount of solar radiation at low latitudes and thus strengthening the intensity of the EASM and increasing summer precipitation in northern China[59,62,63]. However, our results show that some periods of high paleolake water levels in NE Tibet correspond to low 405-kyr eccentricity periods (Fig. 4), which may indicate that precession-induced low-latitude insolation variability plays a secondary role in the paleolake evolutions in the Guide Basin. Jin et al.[62] suggested that there was a short eccentricity-control on hydroclimate records in the Nima Basin of the Tibetan Plateau interior over ~27.32–23.24 million years ago, with precipitation being modulated by low-latitude summer insolation variability rather than glacial-interglacial Antarctic ice sheet fluctuations. However, tuning paleoclimatic proxy records to the 405-kyr orbital curve may cause large phase deviations between the benthic $\delta^{18}O$ (‰) record and the paleoclimatic proxy in question on the ~100-kyr eccentricity scale, an important consideration for records from the Nima Basin. In fact, for Northern Hemisphere ice-free periods from the latest Eocene to the late Pliocene, global climate variability was substantially influenced by Southern Hemisphere summer insolation, amplified by a dynamic Antarctic ice sheet[64].

After the middle Miocene Climate transition, increases in lake levels occurred in the NE Tibetan Guide and Ili basins (Figs. 2 and 4), with maximum lake levels found at about 11–10.5 million years ago[32,55]. Although the Mn/Fe and smectite/(illite+chlorite) show a relatively weak response to the overall rise of water level at 11–10.5 million years ago, the changes of lithology, MS, redness, and Sr content at ~11–10.5 Ma point to a substantial rise in water level at 11–10.5 million years ago[32]. Provenance[65] and paleomagnetic[38] studies suggest that the Guide Basin was not significantly impacted by renewed uplift until ~8 million years ago, after the deposition of the lacustrine Ashigong Formation. It is particularly noteworthy that the 11.4–10.5 million years ago time window corresponds very well to the peak of Asian monsoonal intensity during the Neogene[66]. Stable isotopes from the South China Sea indicate a remarkable warming episode at ~10.8–10.7 million years ago[67], which fits with maximum lake expansion in our section. We thus argue that climate changes, rather than tectonic activity, are the most likely driver of water level fluctuations during this time. In addition, this period (11−10 million years ago) of lake expansion not only occurred in the Guide Basin, but also in the adjacent Xunhua and Linxia basins[31]. Therefore, this is not a local event, but a common phenomenon in several NE Tibetan basins.

The intensity of chemical weathering in the South China also strengthened after the middle Miocene Climate transition, with an extended period of elevated monsoon intensity around 18-10 million years ago, followed by a weakening of the East Asian summer monsoon[30] (Fig. 4). These results may indicate that spatial differences of precipitation variability occurred across Asia after the middle Miocene Climate transition[25,27]. The decrease in atmospheric CO_2 concentrations after the middle Miocene Climate transition, which was accompanied by a decline in global temperature, will generally reduce the amount of water vapor in the atmosphere. This could have led to a long-term intensification of Central Asian aridity and/or precipitation decrease in East Asia, as is suggested by pollen records that are sensitive to pCO_2 variability. However, atmospheric CO_2 is not the only potential control on the Miocene climate of East Asia. Specifically, the expansion of the East Antarctic ice sheet could amplify the interhemispheric temperature gradient, and thus shift tropical rain belts northward into the warmer hemisphere[13,68]. This could produce an overall increase in Northern

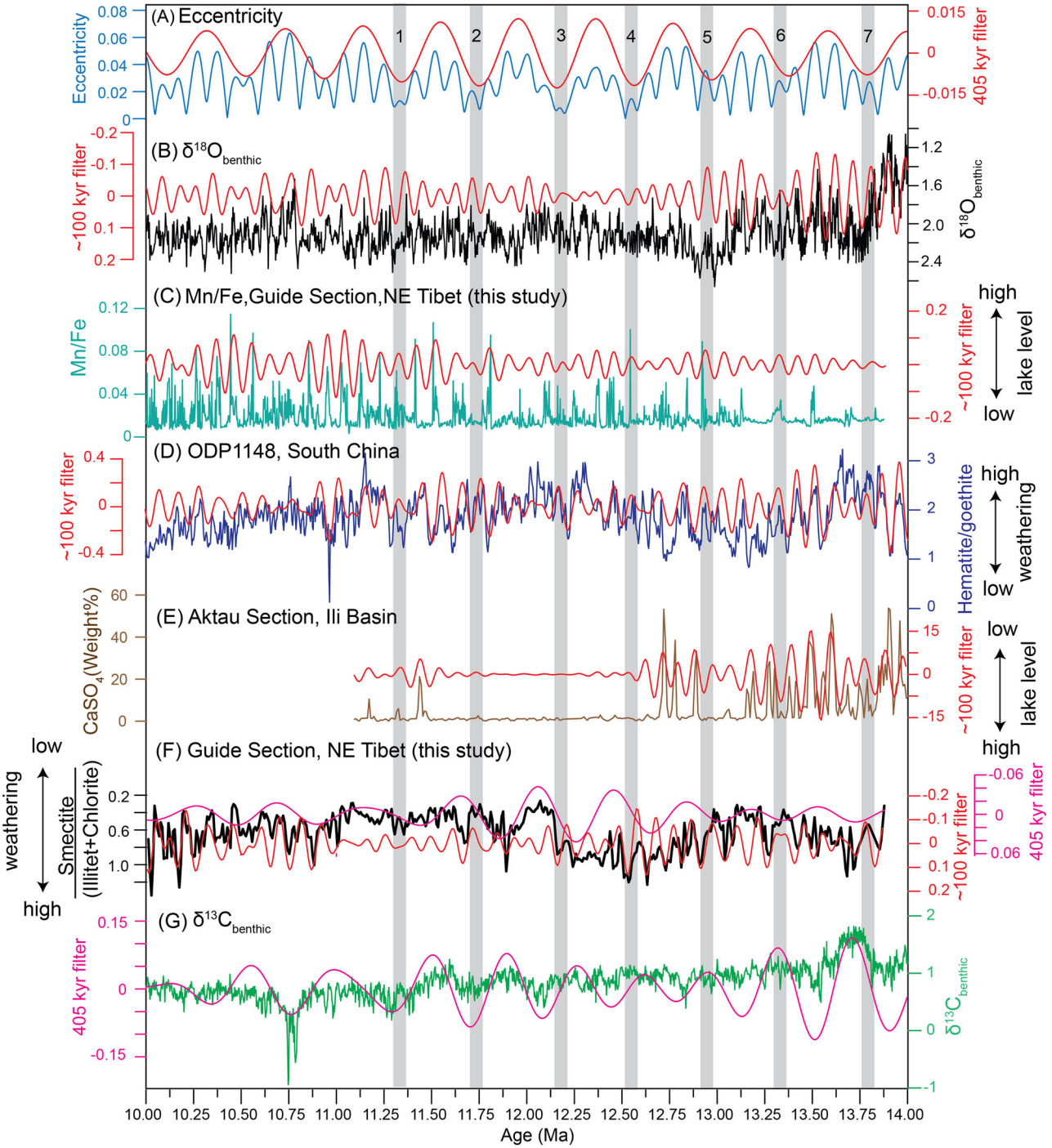

Fig. 4 | Spectral and filter analysis from the Guide Basin in the NE Tibet (this study), and comparison with other climatic records over the interval of 14–10 Ma. A Calculated eccentricity curve with a 405-kyr filter[85] (red curve, 0.0025 ± 0.0005 cycles/kyr). **B** Global $\delta^{18}O_{benthic}$ data with a 100-kyr filter[64] (red curve, 0.01 ± 0.003 cycles/kyr). **C** Mn/Fe ratios in the Guide Basin with a 100-kyr filter (red curve, 0.01 ± 0.003 cycles/kyr). **D** Hematite/goethite ratios from the ODP1148 in the South China Sea with a 100-kyr filter[30] (red curve, 0.01 ± 0.003 cycles/kyr). **E** $CaSO_4$ content from the Aktau section in the Ili Basin and the 100-kyr filter[55] (red curve, 0.01 ± 0.003 cycles/kyr). **F** Smectite/(illite+chlorite) ratios in the Guide section with 405-kyr (pink curve, 0.0025 ± 0.0005 cycles/kyr) and 100-kyr (red curve, 0.01 ± 0.003 cycles/kyr) filters. **G** Global $\delta^{13}C_{benthic}$ data with a 405-kyr filter[72] (pink curve, 0.0025 ± 0.0005 cycles/kyr). The grey bars indicate relatively low values of the theoretical 405-kyr eccentricity.

Hemisphere precipitation[69]. In addition, after the middle Miocene Climate transition, a more vigorous meridional overturning circulation in the Pacific Ocean and intensification of the Atlantic Meridional Overturning Circulation (AMOC) following global cooling occurred due to increased production of circumpolar deep water as well as waters equivalent to modern Antarctic Intermediate Water[14]. Intensified AMOC, and generally enhanced overturning globally, would trigger a growth in northward oceanic heat transport, resulting in Northern Hemispheric warming and elevated rainfall in NE Tibetan basins[22,69].

Climate model results for the Middle Miocene[37] show that the scale of Central Asian aridity induced by the combination of decreasing atmospheric CO_2 and expansion of the Antarctic ice sheet is sensitive to the mean state CO_2 concentration itself (Supplementary Fig. S3). The largest reductions in annual precipitation occur at the lower CO_2 concentrations

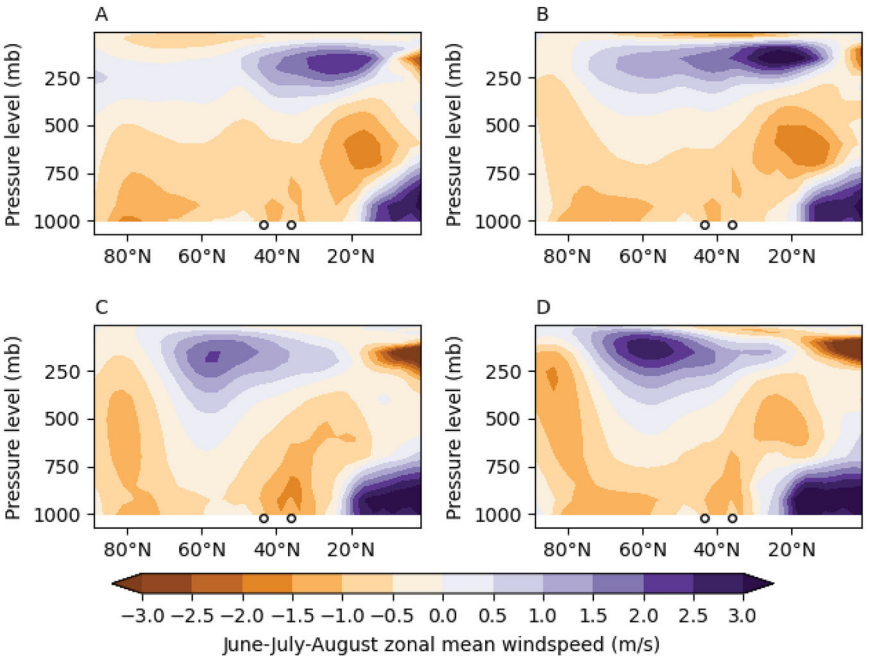

Fig. 5 | Simulated westerly jet position and intensity under Middle Miocene boundary conditions with various orbital configurations favorable for Antarctic ice sheet expansion and retreat at different atmospheric CO_2 concentrations. **A** 280 ppm and an orbital configuration that favors a warmer climate globally without an Antarctic ice sheet. **B** 850 ppm and an orbital configuration that favors a warmer climate globally without an Antarctic ice sheet. **C** 280 ppm and an orbital configuration that favors a cooler climate globally with an Antarctic ice sheet. **D** 850 ppm and an orbital configuration that favors a cooler climate globally with an Antarctic ice sheet. The purple regions in these latitudinal cross-sections through the atmosphere at the ~200 mb pressure levels show the position of the westerlies. The latitudinal positions of the Aktau Section and the Guide Section are shown as white circles.

simulated (Supplementary Fig. S3A). However, at higher simulated CO_2 concentrations, Central Asia becomes wetter as CO_2 decreases (Supplementary. Fig S3C). These results suggest that when Central Asian aridification did take place, atmospheric CO_2 must have been comparatively low. The most recent estimates for the CO_2 decrease over the middle Miocene Climate transition is from at least 500 ppm to ~400 ppm[12]. We therefore suggest that the most appropriate model simulation comparison for the long-term Middle Miocene hydroclimate evolution in Central Asia over our period of interest is Supplementary Fig. S3B (relatively higher atmospheric CO_2), which suggests an overall increase in annual precipitation in this region of ~5-10%. These previous studies, along with our new records, suggest there might be no long-term drying trend across ~14-10 million years ago in NE Tibetan basins. Considering the data and modeling results, we hypothesize that aridification instead occurred after this interval, and was driven by a combination of further reductions in atmospheric CO_2, and the eventual glaciation of Greenland and other regions of the high-latitude Northern Hemisphere. The loss of the Paratethys likely removed an important moisture source[70], while the development of continental ice sheets in the Northern Hemisphere may have altered the position of the westerly jet[71].

Eccentricity-driven variations in moisture sources for NE Tibet may be the cause of the ~100-kyr cycles after the middle Miocene Climate transition. Specifically, higher lake levels occurred in the Guide and Ili Basins[55] during maximum values of eccentricity, generally consistent with lower global $\delta^{18}O$ values, indicating warmer climate intervals (Fig. 4). However, during these warm periods, East Asian continental weathering intensity (and the strength of the East Asian monsoon) was predominantly weaker (shaded intervals 1, 4, 5 and 6 in Fig. 4), although there are some periods of enhanced weathering/summer monsoon strength (shaded intervals 2 and 3 in Fig. 4). Climate model simulations with orbital configurations favorable for Antarctic ice sheet expansion and contraction[37] show that in the warmer climate/ice sheet retreat cases, East Asian monsoon weakening occurs relative to the colder climate/ice sheet expansion cases, regardless of the atmospheric CO_2 concentration (Supplementary Fig. S4A and S4B compared to S4C and S4D). As such, at least on ~100-kyr timescales after the middle Miocene Climate transition, the variations of lake levels in NE Tibet are not synchronized with weathering intensity fluctuations in southern China. This may indicate that moisture derived from the westerlies provided an important contribution to NE Tibetan precipitation during eccentricity maximum over ~14–10 million years ago, an interpretation supported by the correspondence between the Guide and Ili Basins and the climate model simulations for the Middle Miocene[37] that indicate that the position of the Northern Hemisphere westerly jet shifts to the north when the Antarctica ice sheet expands (Fig. 5). We recognize that additional summer monsoonal moisture from the South China Sea and Pacific Ocean to NE Tibet also contributed to overall precipitation on 100-kyr timescales, as evidenced by some correspondence between the hematite/goethite ratios from ODP 1148 and higher smectite/(illite+chlorite) ratios from the Guide Section (shaded interval 3 in Fig. 4; Fig. S5). Despite previous studies suggesting that long-term (~405 kyr) shifts in the global carbon cycle (Fig. 4) and associated global temperature variations triggered long-term changes in the chemical weathering intensity across the continents[72], such similar fluctuations between Mn/Fe ratios and the smectite/(illite+chlorite) in our records suggest that precipitation substantially contributes to variability in chemical weathering, at least on ~100-kyr timescales in East Asia.

Paleoclimatic records and climate model simulations from other studies reveal that a reduced northward migration of the westerlies during the Quaternary alters the timing and duration of the various rainfall intraseasonal stages (namely spring, pre-meiyu, meiyu, and midsummer), resulting in spatial variability in East Asian rainfall[73,74]. Due to the accelerated uplift of the Pamir and Tianshan Mountains in the late Miocene[53,75], the circulation patterns of the westerlies in the Quaternary are likely different from that of the Miocene period. This is because most of water vapor carried by the westerlies is rained out on the windward slope of the Tianshan Mountains and Pamir Plateau today, and thus less moisture can reach NE Tibet since the uplift of the Pamir Mountains[76]. During the Middle Miocene, however, a narrow water-vapor channel may have existed between the Tianshan and Pamir Plateau[53], resulting in more moisture transported to NE Tibet compared to the Quaternary[22]. Our results demonstrate alternating moisture-derived variability between westerly winds and East Asian summer monsoon on the northeastern Tibetan Plateau, potentially related to the waxing and waning of the Antarctic ice sheets on orbital timescales.

Materials and Methods

Data measurement and spectrum analysis

A total of 3700 samples (~10 cm sampling resolution) were collected after removal of the weathered outcrop surface (this removed surface corresponds to a minimum of the uppermost 0.5 m). Ages of the samples are based on the age model of Wang et al.[32]. Approximately 5 g of each sample were ground into powder and passed through a 200-mesh sieve.

To determine the abundance of Fe and Mn, samples were measured by a portable energy-dispersive Innov-X Systems X-ray fluorescence spectrometer in geochemistry mode using beam 1 (50 kv) and beam (10 kv) at the Chinese University of Geoscience (Wuhan). The measurement time for each sample was at least 50 s, taking the average value of three measurements. About 0.5 g of each powdered sample was further sieved using a 150-mesh screen, and mineral contents were subsequently determined using a Olympus Terra BTX II X-Ray Diffraction Analyzer at the Chinese University of Geoscience (Wuhan). The measurement time for each sample was at least 25 min. The compiled $\delta^{18}O_{benthic}$ and $\delta^{13}C_{benthic}$ data are derived from nine $\delta^{18}O_{benthic}$ and $\delta^{13}C_{benthic}$ records[64,72], with an average temporal resolution of 2.89 kyr and 2.80 kyr, respectively.

We calculated the phase relationships between Mn/Fe-$\delta^{18}O_{benthic}$, Mn/Fe-$\delta^{13}C_{benthic}$, and hematite/goethite-smectite/(illite+chlorite) using a cross-spectrum fast Fourier transform, implemented in the IRISSeismic package in R[77]. We calculated the cross spectra using a 200-kyr sliding window and a 10-kyr step size in individual datasets. Phase analysis calculated at the ~100 kyr eccentricity scale was chosen for a frequency range of 90–135 kyr with the highest frequency coherence. The R code is taken from De Vleeschouwer et al.[72]. Evolutionary spectral analysis was carried out using evolutionary Fast Fourier transform spectrograms with *evofft.m* software[78], with a window of 800 kyr and simulation step size of 6 kyr. The ~100 kyr eccentricity components were extracted using Gaussian band-pass filtering in *AnalySeries 2.0.8*[79], with a center frequency and bandwidth of 0.01 and 0.003 cycles/kyr, respectively.

Model simulations

The climate model simulations use the fully coupled atmosphere–ocean GCM HadCM3LB-M2.1aE[80] with the interactive vegetation model TRIFFID[81]. This is the low-resolution ocean version of HadCM3[82], and both the atmosphere and the ocean components have a resolution of 2.5° latitude by 3.75° longitude. The paleogeography used[83] is representative of Middle Miocene conditions with an open Panama Gateway and Indonesian Seaway and a closed Bering Strait. The Tibetan Plateau, the Andes and Greenland are more than 2000 m lower than modern, and Greenland is also ice-free. Simulations were conducted with Antarctica being either ice-free or with a modern-like ice sheet configuration of 55 m sea level equivalent. Where orbital parameters have been altered, they represent a cold orbital configuration favorable for Antarctic glaciation (low obliquity (22.1°), high eccentricity (0.054), perihelion during boreal summer, 374 W m^{-2} summer insolation at 70° S) and a warm orbital configuration favorable for Antarctic deglaciation (high obliquity (24.5°), high eccentricity (0.054), perihelion during austral summer, 483 W m^{-2} summer insolation at 70° S). See Bradshaw et al.[37] for full details of the model setup.

Data availability

Additional data figures and tables can be found in the Supplementary Information. Data generated in this study are available in the figshare website (available from https://doi.org/10.4121/bca22ec1-32e3-4eed-826b-509c621be7bc; Z. Wang[84]). Source data are provided with this paper.

Received: 17 March 2024; Accepted: 18 September 2024;
Published online: 03 October 2024

References

1. Bruch, A. A., Utescher, T. & Mosbrugger, V. Precipitation patterns in the Miocene of Central Europe and the development of continentality. *Palaeogeogr. Palaeoclimatol. Palaeoecol.* **304**, 202–211 (2011).
2. Pound, M. J., Haywood, A. M., Salzmann, U. & Riding, J. B. Global vegetation dynamics and latitudinal temperature gradients during the Mid to Late Miocene (15.97–5.33 Ma). *Earth-Sci. Rev.* **112**, 1–22 (2012).
3. Hui, Z. et al. Global warming and rainfall: Lessons from an analysis of Mid-Miocene climate data. *Palaeogeogr. Palaeoclimatol. Palaeoecol.* **512**, 106–117 (2018).
4. Westerhold, T. et al. An astronomically dated record of Earth's climate and its predictability over the last 66 million years. *Science* **369**, 1383–1387 (2020).
5. De Boer, B., Van de Wal, R., Bintanja, R., Lourens, L. & Tuenter, E. Cenozoic global ice-volume and temperature simulations with 1-D ice-sheet models forced by benthic $\delta^{18}O$ records. *Ann. Glaciol.* **51**, 23–33 (2010).
6. Lear C. H., Mawbey E. M. & Rosenthal, Y. Cenozoic benthic foraminiferal Mg/Ca and Li/Ca records: Toward unlocking temperatures and saturation states. *Paleoceanography* **25**, https://doi.org/10.1029/2009PA001880 (2010).
7. Miller, K. G. et al. Cenozoic sea-level and cryospheric evolution from deep-sea geochemical and continental margin records. *Sci. Adv.* **6**, eaaz1346 (2020).
8. Shevenell, A. E., Kennett, J. P. & Lea, D. W. Middle Miocene southern ocean cooling and Antarctic cryosphere expansion. *Science* **305**, 1766–1770 (2004).
9. Holbourn, A., Kuhnt, W., Schulz, M., Flores, J.-A. & Andersen, N. Orbitally-paced climate evolution during the middle Miocene "Monterey" carbon-isotope excursion. *Earth Planet. Sci. Lett.* **261**, 534–550 (2007).
10. Rousselle, G., Beltran, C., Sicre, M.-A., Raffi, I. & De Rafélis, M. Changes in sea-surface conditions in the Equatorial Pacific during the middle Miocene–Pliocene as inferred from coccolith geochemistry. *Earth Planet. Sci. Lett.* **361**, 412–421 (2013).
11. Super, J. R. et al. North Atlantic temperature and pCO_2 coupling in the early-middle Miocene. *Geology* **46**, 519–522 (2018).
12. The Cenozoic CO_2 proxy Integration Project (CenCO_2Pip) Consortium, Toward a Cenozoic history of atmospheric CO_2. *Science* **382**, https://doi.org/10.1126/science.adi5177 (2023).
13. Holbourn, A. et al. Does Antarctic glaciation force migration of the tropical rain belt? *Geology* **38**, 783–786 (2010).
14. Holbourn, A., Kuhnt, W., Kochhann, K. G., Matsuzaki, K. M. & Andersen, N. Middle Miocene climate–carbon cycle dynamics: Keys for understanding future trends on a warmer Earth?, in I.W. Aiello, J.A. Barron and A.C. Ravelo, eds., Understanding the Monterey Formation and Similar Biosiliceous Units across Space and Time, Geological Society of America Special Paper 556, https://doi.org/10.1130/2022.2556(05) (2022).
15. Lewis, A. R. et al. Mid-Miocene cooling and the extinction of tundra in continental Antarctica. *Proc. Natl Acad. Sci. USA* **105**, 10676–10680 (2008).
16. Steinthorsdottir, M. et al. The Miocene: The Future of the Past. *Paleoceanogr. Paleoclimatol.* **36**, e2020PA004037 (2020).
17. Holbourn, A., Kuhnt, W., Schulz, M. & Erlenkeuser, H. Impacts of orbital forcing and atmospheric carbon dioxide on Miocene ice-sheet expansion. *Nature* **438**, 483–487 (2005).
18. Knorr, G. & Lohmann, G. Climate warming during Antarctic ice sheet expansion at the Middle Miocene transition. *Nat. Geosci.* **7**, 376–381 (2014).
19. Holbourn, A. et al. Middle Miocene climate cooling linked to intensification of eastern equatorial Pacific upwelling. *Geology* **42**, 19–22 (2014).
20. Super, J. R. et al. Miocene Evolution of North Atlantic Sea Surface Temperature. *Paleoceanogr. Paleoclimatol.* **35**, e2019PA003748 (2020).
21. Nie, J. et al. Dominant 100,000-year precipitation cyclicity in a late Miocene lake from northeast Tibet. *Sci. Adv.* **3**, e1600762 (2017).
22. Wang, Z., Huang, C., Licht, A., Zhang, R. & Kemp, D. B. Middle to late Miocene eccentricity forcing on lake expansion in NE Tibet. *Geophys. Res. Lett.* **46**, 6926–6935 (2019).

23. Rohling, E. J. et al. Sea level and deep-sea temperature reconstructions suggest quasi-stable states and critical transitions over the past 40 million years. *Sci. Adv.* **7**, eabf5326 (2021).
24. Hui, Z. et al. Miocene vegetation and climatic changes reconstructed from a sporopollen record of the Tianshui Basin, NE Tibetan Plateau. *Palaeogeogr. Palaeoclimatol. Palaeoecol.* **308**, 373–382 (2011).
25. Miao, Y. et al. Miocene pollen record of KC-1 core in the Qaidam Basin, NE Tibetan Plateau and implications for evolution of the East Asian monsoon. *Palaeogeogr. Palaeoclimatol. Palaeoecol.* **299**, 30–38 (2011).
26. Qiang, X. et al. New eolian red clay sequence on the western Chinese Loess Plateau linked to onset of Asian desertification about 25 Ma ago. *Sci. China Earth Sci.* **54**, 136–144 (2011).
27. Zan, J., Fang, X., Yan, M., Zhang, W. & Lu, Y. Lithologic and rock magnetic evidence for the Mid-Miocene Climatic Optimum recorded in the sedimentary archive of the Xining Basin, NE Tibetan Plateau. *Palaeogeogr. Palaeoclimatol. Palaeoecol.* **431**, 6–14 (2015).
28. Song, C. et al. Middle Miocene to earliest Pliocene sedimentological and geochemical records of climate change in the western Qaidam Basin on the NE Tibetan Plateau. *Palaeogeogr. Palaeoclimatol. Palaeoecol.* **395**, 67–76 (2014).
29. Zhuang, G., Hourigan, J. K., Koch, P. L., Ritts, B. D. & Kent-Corson, M. L. Isotopic constraints on intensified aridity in Central Asia around 12Ma. *Earth Planet. Sci. Lett.* **312**, 152–163 (2011).
30. Clift, P. D., Wan, S. & Blusztajn, J. Reconstructing chemical weathering, physical erosion and monsoon intensity since 25Ma in the northern South China Sea: A review of competing proxies. *Earth Sci. Rev.* **130**, 86–102 (2014).
31. Hough, B. G., Garzione, C. N., Wang, Z. & Lease, R. O. Timing and spatial patterns of basin segmentation and climate change in northeastern Tibet. *Spec. Pap. Geol. Soc. Am.* **507**, 129–153 (2014).
32. Wang, Z., Shen, Y., Licht, A. & Huang, C. Cyclostratigraphy and Magnetostratigraphy of the Middle Miocene Ashigong Formation, Guide Basin, China, and Its Implications for the Paleoclimatic Evolution of NE Tibet. *Paleoceanogr. Paleoclimatol.* **33**, 1066–1085 (2018).
33. Shi, F. et al. Impacts of extremely asymmetrical polar ice sheets on the East Asian summer monsoon during the MIS-13 interglacial. *Quat. Sci. Rev.* **230**, 106164 (2020).
34. Khan, A. A., Zan, J., Fang, X., Zhang, W. & Jadoon, U. F. Global warming drove the Mid-Miocene climate humidification in the northern Tibetan Plateau. *Glob. Planet. Change* **226**, 104135 (2023).
35. Zhang, Y. et al. Cenozoic record of aeolian sediment accumulation and aridification from Lanzhou, China, driven by Tibetan Plateau uplift and global climate. *Glob. Planet. Change* **120**, 1–15 (2014).
36. Wang, X. et al. Parathethys Last Gasp in Central Asia and Late Oligocene Accelerated Uplift of the Pamirs. *Geophys Res Lett.* **46**, 11773–11781 (2019).
37. Bradshaw, C. D. et al. Hydrological impact of Middle Miocene Antarctic ice-free areas coupled to deep ocean temperatures. *Nat. Geosci.* **14**, 429–436 (2021).
38. Fang, X. et al. Late Cenozoic deformation and uplift of the NE Tibetan Plateau: Evidence from high-resolution magnetostratigraphy of the Guide Basin, Qinghai Province, China. *Geol. Soc. Am. Bull.* **117**, 1208–1225 (2005).
39. Yao, X., Dai, S., Wang Z., Li, M., Hinnov, L. Astronomical influence on Miocene continental environments in Tibet, east-central Asia. Geological Society of America Bulletin, https://doi.org/10.1130/B37129.1 (2024).
40. Canfield, D.E. Organic matter oxidation in marine sediments. In: Wollast, R., Mackenzie, F.T., Chou, L. (Eds.), Interactions of C, N, P and S Biogeochemical Cycles and Global Change. Springer, Berlin, pp. 333–363 (1993).
41. Unkel, I., Fernandez, M., Björck, S., Ljung, K. & Wohlfarth, B. Records of environmental changes during the Holocene from Isla de los Estados (54.4°S), southeastern Tierra del Fuego. *Glob. Planet. Change* **74**, 99–113 (2010).
42. Evans, G., Augustinus, P., Gadd, P., Zawadzki, A. & Ditchfield, A. A multi-proxy μ-XRF inferred lake sediment record of environmental change spanning the last ca. 2230 years from Lake Kanono, Northland, New Zealand. *Quat. Sci. Rev.* **225**, 106000 (2019).
43. Ao, H., Deng, C., Dekkers, M. J. & Liu, Q. Magnetic mineral dissolution in Pleistocene fluvio-lacustrine sediments, Nihewan Basin (North China). *Earth Planet. Sci. Lett.* **292**, 191–200 (2010).
44. Yang, R. et al. Late Miocene intensified tectonic uplift and climatic aridification on the northeastern Tibetan Plateau: evidence from clay mineralogical and geochemical records in the Xining Basin. *Geochem. Geophys. Geosyst.* **20**, 829–851 (2019).
45. Fang, X. et al. Paleogene global cooling–induced temperature feedback on chemical weathering, as recorded in the northern Tibetan Plateau. *Geology* **47**, 992–996 (2019).
46. Weaver, C. E. Shale-slate metamorphism in southern Appalachians. *Amst.: Elsevier* **10**, 1–239 (1984).
47. Caves Rugenstein, J. K. & Chamberlain, C. P. The evolution of hydroclimate in Asia over the Cenozoic: A stable-isotope perspective. *Earth Sci. Rev.* **185**, 1129–1156 (2018).
48. Caves, J. K. et al. Role of the westerlies in Central Asia climate over the Cenozoic. *Earth Planet. Sci. Lett.* **428**, 33–43 (2015).
49. Bookhagen, B., Thiede, R. C. & Strecker, M. R. Abnormal monsoon years and their control on erosion and sediment flux in the high, arid northwest Himalaya. *Earth Planet. Sci. Lett.* **231**, 131–146 (2005).
50. Miao, Y. F. et al. Late Cenozoic continuous aridification in the western Qaidam Basin: evidence from sporopollen records. *Climate* **9**, 1863–1877 (2013).
51. Guo, Z. T. et al. Onset of Asian desertification by 22 Myr ago inferred from loess deposits in China. *Nature* **416**, 159–163 (2002).
52. Sobel, E., Chen, J. & Heermance, R. Late Oligocene–Early Miocene initiation of shortening in the Southwestern Chinese Tian Shan: Implications for Neogene shortening rate variations. *Earth Planet. Sci. Lett.* **247**, 70–81 (2006).
53. Sun, J. et al. Extreme aridification since the beginning of the Pliocene in the Tarim Basin, western China. *Palaeogeogr. Palaeoclimatol. Palaeoecol.* **485**, 189–200 (2017).
54. Sun, Y. et al. Mid-Miocene sea level altitude of the Qaidam Basin, northern Tibetan Plateau. *Commun. Earth Environ.* **4**, 3 (2023).
55. Frisch, K. et al. Long-Period Astronomical Forcing of Westerlies' Strength in Central Asia During Miocene Climate Cooling. *Paleoceanogr. Paleoclimatol.* **34**, 1784–1806 (2019).
56. Zhang, Y. G., Ji, J., Balsam, W. L., Liu, L. & Chen, J. High resolution hematite and goethite records from ODP 1143, South China Sea: Co-evolution of monsoonal precipitation and El Niño over the past 600,000 years. *Earth Planet. Sci. Lett.* **264**, 136–150 (2007).
57. Zhang, Y. G., Ji, J., Balsam, W., Liu, L. & Chen, J. Mid-Pliocene Asian monsoon intensification and the onset of Northern Hemisphere glaciation. *Geology* **37**, 599–602 (2009).
58. Sun, Y., Clemens, S. C., An, Z. & Yu, Z. Astronomical timescale and palaeoclimatic implication of stacked 3.6-Myr monsoon records from the Chinese Loess Plateau. *Quat. Sci. Rev.* **25**, 33–48 (2006).
59. Wang, Y. et al. Combined high-and low-latitude forcing of East Asian monsoon precipitation variability in the Pliocene warm period. *Sci. Adv.* **6**, eabc2414 (2020).
60. Zhang, Z. et al. East Asian monsoonal climate sensitivity changed in the late Pliocene in response to Northern Hemisphere glaciations. *Geophys. Res. Lett.* **49**, e2022GL101280 (2022).
61. Ao, H. et al. Eccentricity-paced monsoon variability on the northeastern Tibetan Plateau in the Late Oligocene high CO_2 world. *Sci. Adv.* **7**, eabk2318 (2021).
62. Jin, C.-S. et al. Tectonic and orbital forcing of the South Asian monsoon in central Tibet during the late Oligocene. *Proc. Natl Acad. Sci. USA* **120**, e2214558120 (2023).

63. Liu, C. et al. Eccentricity forcing of East Asian monsoonal systems over the past 3 million years. *Proc. Natl Acad. Sci. USA* **118**, e2107055118 (2021).
64. De Vleeschouwer, D., Vahlenkamp, M., Crucifix, M. & Pälike, H. Alternating Southern and Northern Hemisphere climate response to astronomical forcing during the past 35 m.y. *Geology* **45**, 375–378 (2017).
65. Lease, R. O., Burbank, D. W., Gehrels, G. E., Wang, Z. & Yuan, D. Signatures of mountain building: Detrital zircon U/Pb ages from northeastern Tibet. *Geology* **35**, 239–242 (2007).
66. Clift, P. D. et al. Correlation of Himalayan exhumation rates and Asian monsoon intensity. *Nat. Geosci.* **1**, 875–880 (2008).
67. Holbourn, A., Kuhnt, W., Frank, M. & Haley, B. A. Changes in Pacific Ocean circulation following the Miocene onset of permanent Antarctic ice cover. *Earth Planet. Sci. Lett.* **365**, 38–50 (2013).
68. Hyeong, K. et al. Southward shift of the Intertropical Convergence Zone due to Northern Hemisphere cooling at the Oligocene-Miocene boundary. *Geology* **42**, 667–670 (2014).
69. Zhao, S. et al. Responses of the East Asian summer monsoon in the low-latitude South China Sea to high-latitude millennial-scale climatic changes during the last glaciation: Evidence from a high-resolution clay mineralogical record. *Paleoceanogr. Paleoclimatol.* **33**, 745–765 (2018).
70. Zhang, Z., Wang, H., Guo, Z. & Jiang, D. What triggers the transition of palaeoenvironmental patterns in China, the Tibetan Plateau uplift or the Paratethys Sea retreat? *Palaeogeogr. Palaeoclimatol. Palaeoecol.* **245**, 317–331 (2007).
71. Abell, J. T., Winckler, G., Anderson, R. F. & Herbert, T. D. Poleward and weakened westerlies during Pliocene warmth. *Nature* **589**, 70–75 (2021).
72. De Vleeschouwer, D. et al. High-latitude biomes and rock weathering mediate climate–carbon cycle feedbacks on eccentricity timescales. *Nat. Commun.* **11**, 5013 (2020).
73. Chiang, J. C. H. et al. Role of seasonal transitions and westerly jets in East Asian paleoclimate. *Quat. Sci. Rev.* **108**, 111–129 (2015).
74. Herzschuh, U. et al. Position and orientation of the westerly jet determined Holocene rainfall patterns in China. *Nat. Commun.* **10**, 2376 (2019).
75. Zhao, X. et al. Signatures of tectonic-climatic interaction during the Late Cenozoic orogenesis along the northern Chinese Tian Shan. *Basin Res.* **33**, 291–311 (2020).
76. Yang, S. & Ding, Z. A 249 kyr stack of eight loess grain size records from northern China documenting millennial-scale climate variability. *Geochem. Geophys. Geosyst.* **15**, 798–814 (2014).
77. Callahan, J., Casey, R., Sharer, G. & Templeton, M., IRISSeismic: classes and methods for seismic data analysis, (2019).
78. Kodama, K.P. & Hinnov, L. A. Rock magnetic cyclostratigraphy, John Wiley & Sons, https://doi.org/10.1002/9781118561294 (2014).
79. Paillard, D., Labeyrie, L. & Yiou, P. Macintosh program performs time-series analysis. *Eos, Trans. Am. Geophys. Union* **77**, 379–379 (1996).
80. Valdes, P. J. et al. The BRIDGE HadCM3 family of climate models: HadCM3@Bristol v1.0. *Geoscientific Model Dev.* **10**, 3715–3743 (2017).
81. Cox, P. M. Description of the "TRIFFID" dynamic global vegetation model. Technical report, Hadley Centre Tech. Note 24. Bracknell, UK: Hadley Centre. [WWW document] URL https://jules.jchmr.org/sites/default/files/HCTN_24 (2001).
82. Gordon, C. et al. The simulation of SST, sea ice extents and ocean heat transports in a version of the Hadley Centre coupled model without flux adjustments. *Clim. Dyn.* **16**, 147–168 (2000).
83. Markwick, P. J. Deep-Time Perspectives on Climate Change: Marrying the Signal from Computer Models and Biological Proxies. *Geol. Soc. Lond.* **2**, 251–312 (2007).
84. Wang, Z. Data from the Guide Basin in the NE Tibet over the past 13.7-10 Ma (version 1) [Dataset]. 4TU. ResearchData. https://doi.org/10.4121/bca22ec1-32e3-4eed-826b-509c621be7bc (2024).
85. Laskar, J. et al. A long-term numerical solution for the insolation quantities of the Earth. *Astron. Astrophys.* **428**, 261–285 (2004).

Acknowledgements

We thank Deng Yunkai, Li Yanzhen, Li Yanzhi, Shen Yongjin and Tian Wei for their assistance with field sampling. No permissions were required of geological samples. This work was supported by the National Natural Science Foundation of China (42230208), Hubei Province Post-doctoral Innovation Research Station (1232002), and the China Postdoctoral Foundation (2020M682517).

Author contributions

Zhixiang Wang and Catherine D. Bradshaw: Conceptualization, Methodology, Data analysis, Investigation, Writing – original draft, Writing – review and editing. Jordan T. Abell: Data analysis, Investigation, Writing – original draft, Writing – review and editing. Haicheng Wei, Wenxia Han, Chunju Huang and Mengmeng Cao: Funding support, Software, Supervision, Writing – review and editing.

Competing interests

The authors declare no competing interests.

Additional information

Supplementary information The online version contains supplementary material available at https://doi.org/10.1038/s43247-024-01710-2.

Correspondence and requests for materials should be addressed to Zhixiang Wang, Chunju Huang or Wenxia Han.

Peer review information *Communications Earth & Environment* thanks Enqing Huang, Lei Huang and the other, anonymous, reviewer(s) for their contribution to the peer review of this work. Primary Handling Editors: Yiming Wang and Carolina Ortiz Guerrero. A peer review file is available.